Seismo-acoustic gliding: an experimental study

Spina, L.[1], Cannata, A.[2,3], Morgavi, D.[4], Privitera, E.[3], Perugini, D.[4]*

1. *Istituto Nazionale di Geofisica e Vulcanologia, Sezione di Roma1, Rome, Italy.*
2. *Dipartimento di Scienze Biologiche, Geologiche e Ambientali, Università degli Studi di Catania, Catania, Italy*
3. *Istituto Nazionale di Geofisica e Vulcanologia, Osservatorio Etneo, Catania, Italy*
4. *Dipartimento di Fisica e Geologia, Università degli Studi di Perugia, Perugia, Italy*

Abstract

The gradual temporal shift of the spectral lines of harmonic seismic and/or acoustic tremor, known as spectral gliding, has been largely documented at different volcanoes worldwide. Despite the clear advantage of the experimental approach in providing direct observation of degassing processes and related elastic radiation, experimental studies on gliding tremor are lacking. Therefore, we investigated different episodes of gliding of acoustic and seismic tremor observed during analogue degassing experiments performed under different conditions of magma viscosity (10-1,000 Pa s), gas flux (5-180x10^{-3} l/s) and conduit surface roughness (fractal dimension of 2-2.99). Gliding experimental harmonic seismic and acoustic tremor was observed at high gas flux rates and viscosities, mostly associated with an increasing trend and often preceding a major burst. Decreasing secondary sets of harmonic spectral lines were observed in a few cases. Results suggest that gliding episodes are mostly related to the progressive volume variation of shallow interconnected gas pockets. Spectral analyses performed on acoustic signals provided the theoretical length of the resonator that was compared against the temporal evolution of the gas pockets, quantified from video analyses. The similarities between the observed degassing regime and churn-annular flow in high viscous fluids encourages further studies on churn dynamics in volcanic environments.

Keywords: seismo-acoustic gliding, experimental volcanology, churn-like flow, acoustic resonance, volcanic tremor

1. Introduction

Volcanoes generate tremors that are defined as continuous signals with duration of minutes, days or even longer. Volcanic tremor is considered one of the most distinctive signals recorded at a volcano (McNutt and Roman, 2015 and references therein). In most volcanoes worldwide, the energy of volcanic tremor is generally contained in the frequency band 0.5 -10 Hz (e.g. McNutt and Nishimura, 2008 and references therein). Harmonic tremor is a particular type of tremor, whose spectrum is characterized by the presence of regularly spaced peaks, which sometimes gradually change over time giving rise to gliding spectral lines on the spectrograms (e.g. Almendros et al., 2012; Hotovec et al., 2013). This phenomenon, known as gliding, has been observed in many volcanoes worldwide such as Arenal (Hagerty et al., 2000; Almendros et al., 2012), Veniaminof (De Angelis and McNutt, 2007), Semeru (Schlindwein et al., 1995), Lascar (Hellweg, 2000), Montserrat (Neuberg et al., 2000), Redoubt (Hotovec et al., 2013), Reventador (Lees et al., 2008), Sangay (Lees and Ruiz, 2008), Erebus (Rowe et al., 2000) and Stromboli (Ripepe et al., 2009). Gliding has been mainly recorded in the seismic signals, but the cases of observation of seismic-acoustic gliding are increasing in number in the last years (e.g. Johnson and Lees, 2000; Lees et al., 2008; Ichihara et al., 2013). It is also worth noting that gliding with increasing frequency patterns has been observed preceding explosions at some volcanoes such as Arenal (Lesage et al., 2006), Soufrière Hills (Powell and Neuberg, 2003) and Redoubt (Hotovec et al., 2013). Although gliding tremor is quite commonly observed in active volcanoes, its source mechanism is still open to debate (e.g. Hotovec et al., 2013). A wide variety of models have been suggested to explain the generation mechanism of harmonic tremor and the associated gliding phenomena, such as resonance of portions of plumbing system, resonance of gas-filled bubbles, a combination of discrete pulses producing evenly spaced harmonics, non-linear fluid flow and/or non-linear responses to fluid flow (e.g. Chouet, 1985; Hellweg, 2000; Jellinek and Bercovici, 2011; Hotovec et al., 2013). Noteworthy, the assumption of a specific source model for seismo-acoustic harmonic tremor heavily influences the way we decode changes in time and frequency domain, with implication both for monitoring and research purposes.

In this context, analogue laboratory experiments of volcanic processes are a fundamental tool because they incorporate the physics of numerical models with the generation of actual seismo-acoustic observations that can be compared to data from volcanoes (Lyons et al., 2013). Among the plethora of experimental works devoted to the investigation of seismic and acoustic radiation of scaled volcanic degassing processes (e.g. Lane et al., 2001; James et al., 2004; Arciniega et al., 2014), sustained seismic and/or acoustic radiation has been addressed by a relatively smaller number of studies (e.g. Benson et al., 2008; Fazio et al., 2019; Lyons et al., 2013; Spina et al., 2019). Among these, Clarke et al. (2019) found that tremor was observed only in the early stages of low-viscosity fluid venting and hypothesized fast-moving gas as preferential source. The generation of seismic and seismo-acoustic harmonic tremor has been related to the occurrence of stable degassing path of compressed air in high-stiffness visco-elastic fluids in a controlled-valve system by Lyons et al. (2013). More recently, Spina et al. (2019) observed that conduit roughness and analogue magma viscosity influence with opposite trends the power law equation linking squared seismic amplitude of tremor to gas flow rate. Although gliding of the spectral lines can be theoretically predicted by the above mentioned models and experiments and it is quite frequently reported in nature, direct observation of harmonic tremor gliding in laboratory environments is lacking. Here, we aim to overcome this gap by examining several gliding episodes of seismic and acoustic signals generated during scaled analogue experiments. The experiments aim to reproduce different degassing regimes mainly slug and churn to annular flow, that have been commonly assumed to occur in medium to low-viscosity magmas within the shallow conduit (e.g. Vergniolle and Jaupart, 1986; Pioli et al., 2012; Spina et al., 2019). This goal was achieved by injecting controlled air flux (5-180x10^{-3} l/s) in analogue conduits with variable conduit roughness (fractal dimension changing from 2, 2.18 and 2.99) and analogue magma viscosity (10, 100 and 1,000 Pa s; for further detail see Spina et al., 2019). Among the several recordings of seismic and/or acoustic tremor, different episodes of gliding were observed and characterized here by comparing their spectral properties against the temporal evolution of the spatial pattern of the two-phase mixture, performed by image analysis. Our study aims to determine the experimental variables (in other words the degassing condition) that influence the occurrence and evolution of harmonic tremor gliding and the best matching source model valid for the observed degassing processes.

2. Materials and methods

2.1 Data treatment

The experimental setup, used to mimic degassing processes taking place in the upper portion of the volcano plumbing system and the related elastic radiation, is described in detail in Spina et al. (2018; 2019) and in Giudicepietro et al. (2020) and is composed of two parts: i) the analogue conduit, reproducing volcanic degassing phenomena, and ii) the sensor system, used to record the associated accelerometric and acoustic signals. The analogue conduit is made up of a compressor system connected to a set of flow-meters and that allows gas (air) to be injected into epoxy conduits (mean diameter of 3 cm and length of 80 cm) filled with silicone oils (Wacker©, with density of 970 kg/m^3) that act as an analogue for basaltic magma. As for (ii), it consists of a ceramic shear accelerometer ICP J352C33 model (PCB Piezotronics) with a sensitivity of 0.1 V/g in the band 0.5–10,000 Hz, and a microphone ICP 378B02 model (PCB Piezotronics) with a sensitivity of 50 mV/Pa in the band 7–10,000 Hz (±1 dB). The digital acquisition system is a DAS50 (SEFRAM). Both accelerometric and acoustic signals were acquired at a sampling rate of 50 kHz. A video camera recording at 25 fps allowed for visual observation of degassing processes.

A series of experiments, with durations ranging from about 60 to 100 s, were carried out by systematically changing the conditions in terms of roughness of the epoxy conduits, viscosity of the analogue magma and air flow rate. In particular, the roughness of the epoxy conduits, quantified by the fractal dimension (D) of the internal surface, is equal to 2 (smooth conduit, referred to as “C1”), 2.18 (“C2”) and 2.99 (“C3”). For further details, on the protocol implemented to realize fractal epoxy conduit with well-constrained internal geometries, see Spina et al. (2019). Concerning the viscosity, three oil types with viscosity values of 10, 100 and 1,000 Pa s were used. Finally, the air flow rates were fixed to 5, 10, 30, 60, 90, 120, 150, 180×10^{-3} l/s. Hence, 72 (3×3×8) conditions were tested. We additionally included in the dataset some runs with repeated experimental conditions because they exhibited clear or illustrative examples of gliding. After each change of gas flux, we carefully waited several minutes before recording seismo-acoustic signals and video images to ensure stable degassing conditions were achieved. Therefore, hereafter, the zero time of each experimental run represents the starting time of recording after a stable degassing regime has been reached.

2.2 Methods

To extract information on the harmonic patterns producing the gliding phenomena, Short Time Fourier Transform (STFT) was performed on both accelerometric and acoustic signals by using a 1-s-long sliding window, with an overlap of 0.9 s (**Figure 1**). In particular, we focused on the 10-10,000 Hz band, which is the shared band of flat response for both the accelerometer and the microphone. Then, we selected the experiments showing the clearest gliding evidence and for those experiments, in the acoustic spectrograms, we identified a set of evident consecutive harmonics, generally falling in an intermediate frequency range (indeed, the harmonics at low frequency are often hidden by noise, and the ones at high frequency show low amplitudes). Those harmonics are tracked by manually identifying a set of points in the spectrograms, each of which characterized by a pair of time-frequency values. The obtained frequency values are interpolated on an equispaced time scale, common for all the selected harmonics. Then, we compute the frequency spacing Δf between consecutive harmonics at each time step. Finally, the obtained values of Δf for each time step were averaged, to obtain an average length $\overline{L}$ of the resonator at a given time, under the assumption of a closed-closed or open-closed pipe resonator system (**Section 3** for more details). The experimental condition of this subset of experiments is described in **Supplementary Table 1**. Acoustic signals exhibit most clearly and more often gliding episodes and were taken as a reference for this task. It is worth noting that in most cases, due to intense low frequency noise, it was not possible to clearly identify and track the harmonics with lowest frequencies, among which the fundamental mode.

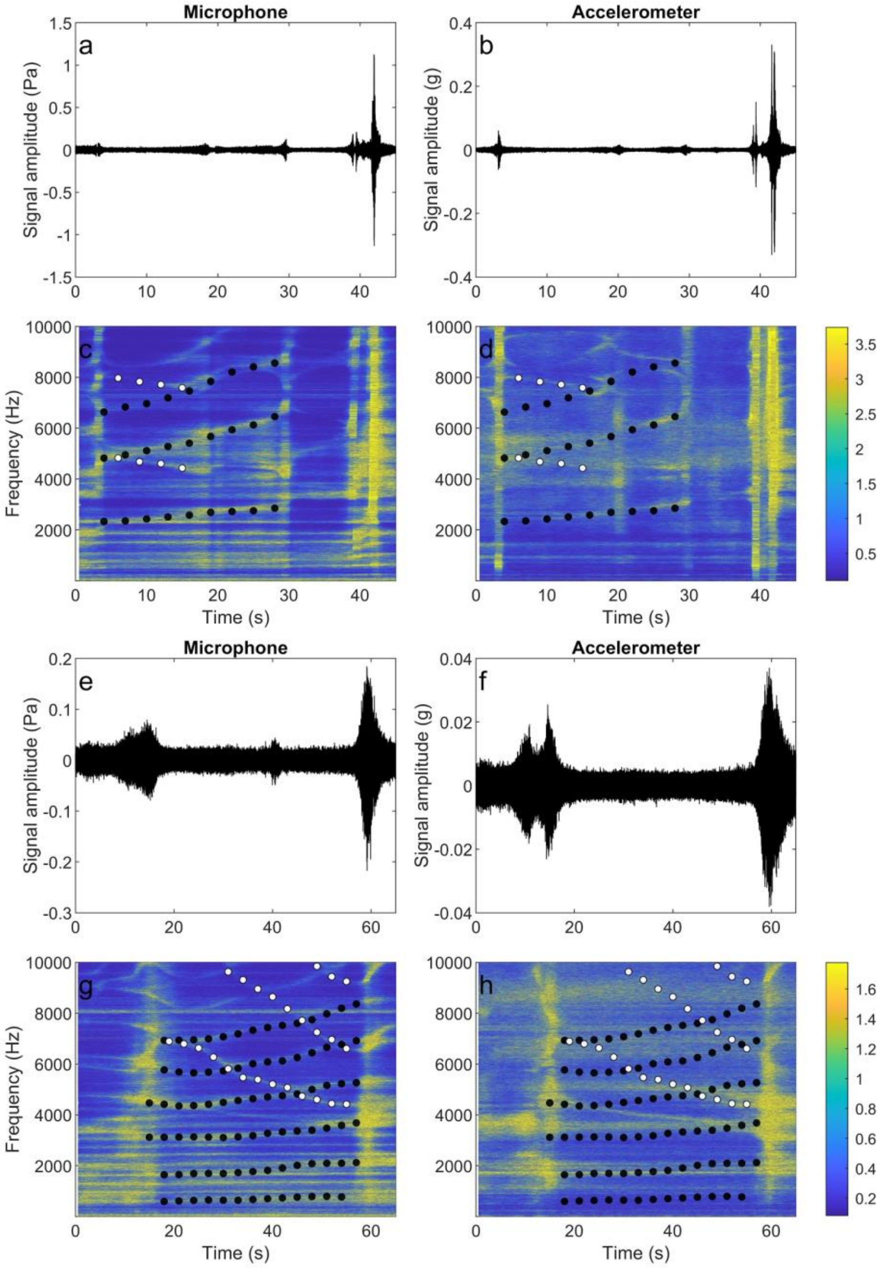

Figure 1*: Examples of signals recorded by microphone (a,e) and accelerometer (b,f) and corresponding spectrograms (c,d,g,h) calculated by using a 1-s-long sliding window, overlapped by 0.9 s. In particular, the signals in (a,b) were recorded during the experiment with the following conditions: roughness C2, silicone oil viscosity of 1,000 Pa s and air flow rate of 120×10^{-3} l/s. The signals in (e,f) during the experiment with the following conditions: roughness C1, silicone oil viscosity of 1,000 Pa s and air flow rate of 180×10^{-3} l/s. The black and white dots in (c,d,g,h) indicate the temporal variations of the most evident harmonics with increasing and decreasing frequency patterns, respectively.*

The parametrization of the degassing regime at different time steps has been performed by analyzing video images by using Tracker© software. In **Figure 2** (a,b,c,d), we show a schematic representation of the analogue conduit at 0, 30, 60 and 90 s, respectively. The light azure color indicates the distribution of the gas phase in the system, mostly featuring a train of connected pockets of gas, whereas white color indicates silicone oil fluids. In order to characterize their spatial and temporal distribution, we focused on two parameters: i) the position of the termination (e.g. points A, B, C and D in **Figure 2**a,b,c,d) and ii) the length of each gas pocket (e.g. segments AB, CA in **Figure 2**a,b,c). These two variables were tracked with a semi-automatic approach; at time zero, the starting key frame, we defined a template area (an image of a feature of interest, that is searched for best matches in the following frames) and a target (the position at which points are marked relative to the template when matches are found). New key frames were defined when very rapid variation of the gas phase distribution caused failure to identify the correct point. The evolution of the investigated points, marking the termination of a gas pocket, is sampled at time steps of 5 frames, as shown in **Figure 2e**. The difference between consecutive termination points provides the length of the gas pocket, as shown in **Figure 2f**.

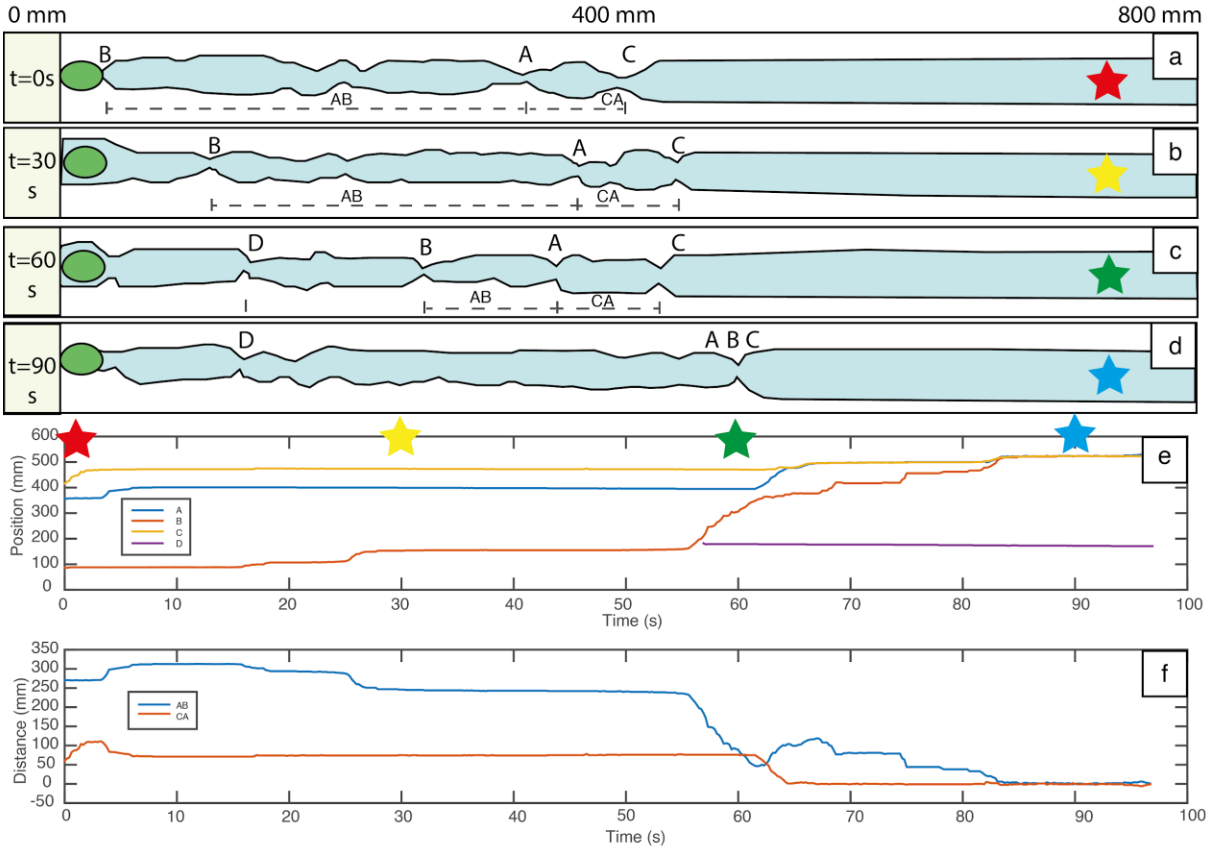

Figure 2: (a,b,c,d) Simplified sketches of gas distribution at different time intervals (0, 30, 60 and 90 seconds, respectively) for an experiment performed with the following conditions: roughness C1, silicone oil viscosity of 1,000 Pa s and air flow rate of 90×10^{-3} l/s. Capital letters mark the termination (A, B, C, D) or the total length (AB, CA) of a gas pocket. Note that the sketches of the conduit in a-d have been rotated of 90 degrees to the right (i.e. the experiments were performed with vertically orientated conduits). The green oval in (a-d) represents the gas injector. (e, f) Analysis of the temporal evolution of gas pockets through video images. Red, yellow, green and blue stars indicate the temporal position of the sketch a, b, c and d. In (e) the position of the different gas pocket terminations is tracked through time, whereas in (f) the length of the gas pockets (i.e. the distance between consecutive gas pocket terminations) is plotted.

3. Results

Harmonic acoustic and seismic tremor has been commonly observed during our experiments, with more clear and stable patterns particularly for high viscosity runs. Acoustic signals exhibited much clear patterns compared to seismic data and were taken as reference for frequencies picking of the spectral lines (**Figure 1**). Stable harmonics might last tens of seconds, quite often they are disrupted by the burst of gas pockets at the surface. In some cases, the explosive release of gas, accompanied by an increase in the amplitude of both accelerometric and acoustic signals, marks the onset for a new series of harmonics. The concurrent variation of the frequency of each spectral line of the harmonics, i.e. a gliding episode, was more often observed to follow a positive (increasing) trend (upward gliding). Secondary sets of gliding harmonics, with smaller spectral amplitudes, were also observed. In several cases, the latter are characterized by a negative (decreasing) pattern of the spectral lines (downward gliding).

In **Figure 3,** we mapped the experimental conditions featuring episodes of gliding of the accelerometric (blue solid square) and acoustic (red empty square) signals, cross-checked with the transition among different regimes as reported in Spina et al. (2019). Slug flow was characterized by the presence of single conduit-filling gas slugs moving upwards, the liquid at the conduit wall moving downward to allow for gas migration (e.g. Pioli et al. 2012). The definition of churn/annular-like flow has been here given according to the following: 1) Direct observation of degassing behavior provided the canonical progression from spherical cap bubble to Taylor bubble characterizing slug flow (e.g. Pering and McGonigle, 2018). Further increases in flow rate induced disruption of the slug regime and a new degassing pattern characterized by gas phase being localized at the core of the system, with the liquid phase intermittently driven up along the conduit wall, as commonly described in churn flow. An additional increase in gas flow rate has been associated to mostly sustained liquid phase at the wall surrounding an open gas core, similarly to annular flow. 2) The motion of liquid phase at the wall of the conduit, alternating downward flow to impulsive and intermittent upward motion resembles the definition of flooding (i.e. the flow is carried upward in large waves; Hewitt et al,. 1985) that is quite typical for churn degassing regime. 3) The description of the degassing pattern corresponds to what provided in Mohammed et al. (2018, 2019) and Hasan et al. (2019) (**Section 4** for more details) for transition to churn flow and churn flow in high viscous fluids. Nevertheless, gas pockets generating harmonic tremor were often observed within 10 diameters D from the gas inlet (D=3 cm, hence within 30 cm); that is conventionally considered the minimum length to achieve fully developed flow. Such intrinsic limitation of the experimental setup could possibly influence the stability of the degassing regime; additionally, the unprecedented high viscosity of the analogue fluids makes difficult direct comparison to very low viscous fluids (as those commonly used in the classical two-phase theory). For such reasons, we use the definition of *churn and annular-like* regime to remark that degassing pattern exhibits several similarities with canonical churn and annular regime.

Gliding tremor has been observed independently from the fractal dimension of the experimental conduit, i.e. conduit roughness does not seem to play a primary role in its generation. Scrutinizing the 24 combinations of gas flux and viscosity here investigated, we found 15 observations of gliding, all distributed in the churn/annular-like flow regime of high-viscosity analogue magmas. Additionally, no episodes of gliding tremor have been associated with experiments performed with 10 Pa s analogue magmas, suggesting that both the degassing pattern and the viscosity of the analogue magma play a relevant role. Experiments performed at 1,000 Pa s display the clearest and most widespread gliding episodes. At 100 Pa s, gliding tremor has been observed in association with very high flux rate (>$120x10^{-3}$ l/s).

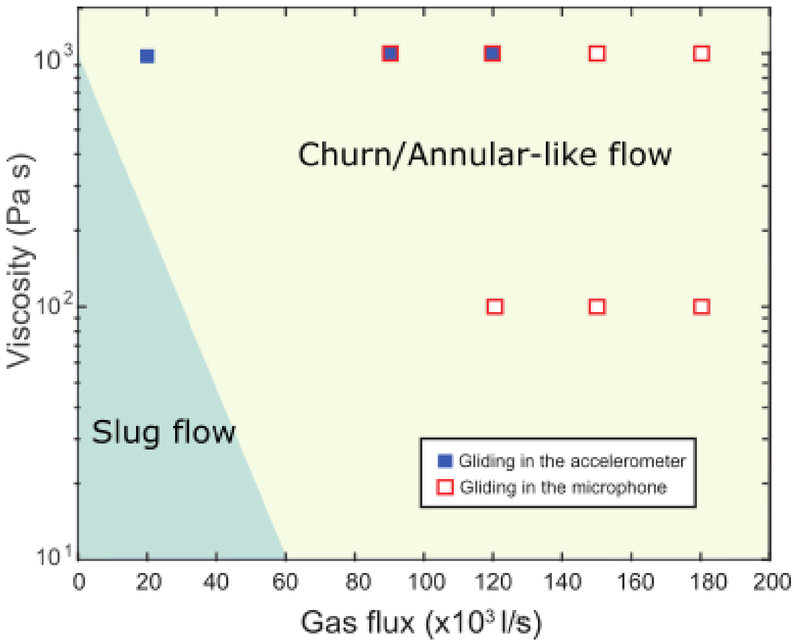

Figure 3*: Experimental conditions (viscosity and gas flux) where spectral gliding was observed. Blue squares correspond to observations of gliding in the accelerometer signal, whereas red empty squares mark gliding episodes in the microphone data. The azure and yellow shadow zones indicate the experimental conditions linked to slug and churn/annular-like degassing regimes by visual observation in Spina et al. (2019). The total number of experiments shown in this graph is equal to 15. Please note that data points overlap at experimental conditions corresponding to: 1) 1,000 Pa s and $180x10^{-3}$ l/s (3 points), 2) 1,000 Pa s and $120x10^{-3}$ l/s (2 points), 3) 1,000 Pa s and 90 $x10^{-3}$ l/s (2 points), 4) 100 Pa s and $180x10^{-3}$ l/s (3 points).*

Therefore, to identify and study the source of gliding tremor, we addressed more strictly the corresponding dynamics of the two-phase analogue system both by visual characterization of the degassing regime and by tracking the evolution in time of spatial parameters such as the position of the termination of individual gas pockets and their length.

At 1,000 Pa s, as schematically represented in **Figure 2a-d**, the two-phase flow consists of different regions of gas pockets, connected to an open core at the outermost section of the analogue conduit. In fact, at the disruption of the slug regime, Taylor bubbles lose their round shape and liquid slugs between bubbles disappear; churn areas are connected to the deformed bubbles by a small neck (Mohammed et al., 2018). The progressive transition from long bubbles (characterizing the high-flow-rate runs at the boundary with the slug flow regime) to the new degassing regime (characterized by over pressurized and interconnected gas pockets) becomes more evident with increasing flow rate. These gas pockets usually move progressively forward, due to their overpressure, until the shallowest one bursts at the top of the liquid column, providing new liquid material above the underlying gas unit. For high flux rate runs (>120x10^{-3} l/s) at 100 Pa s exhibiting gliding tremor the dynamics of gas burst at the surface are much faster than at 1,000 Pa s and characterized by longer bubble and regions of churn-like behavior that are less stable in time. Slug units with similar length of the liquid column have been observed in 100 Pas experiments; this observation implies undeveloped slug flow for this experimental condition, similarly to previously published papers (Hasan et al., 2019).

The evolution of the two-phase flow in time has been mapped by tracking the spatial position of different gas pockets terminations, i.e. points marking either the top or the bottom of gas pocket. **Figures 4** and **5** provide the evolution in time of the position of gas pockets terminations (panel a) and the length of gas pockets (panel b) of the experiments shown in **Figure 1**a-d and **Figure 1**e-h, respectively. The corresponding videos are shown **in Supplementary Videos 1** and **2**. In both cases, we observe an opposite volumetric change of contiguous gas pockets associated with the presence (panel c) of a positive trend of a gliding episode in the primary (i.e. dominant for spectral amplitude) harmonics and of a negative trend in the secondary set of harmonics. **Supplementary Figures 1** to **6** and **Supplementary movies 3** to **8** provide further records of degassing dynamics during gliding episodes.

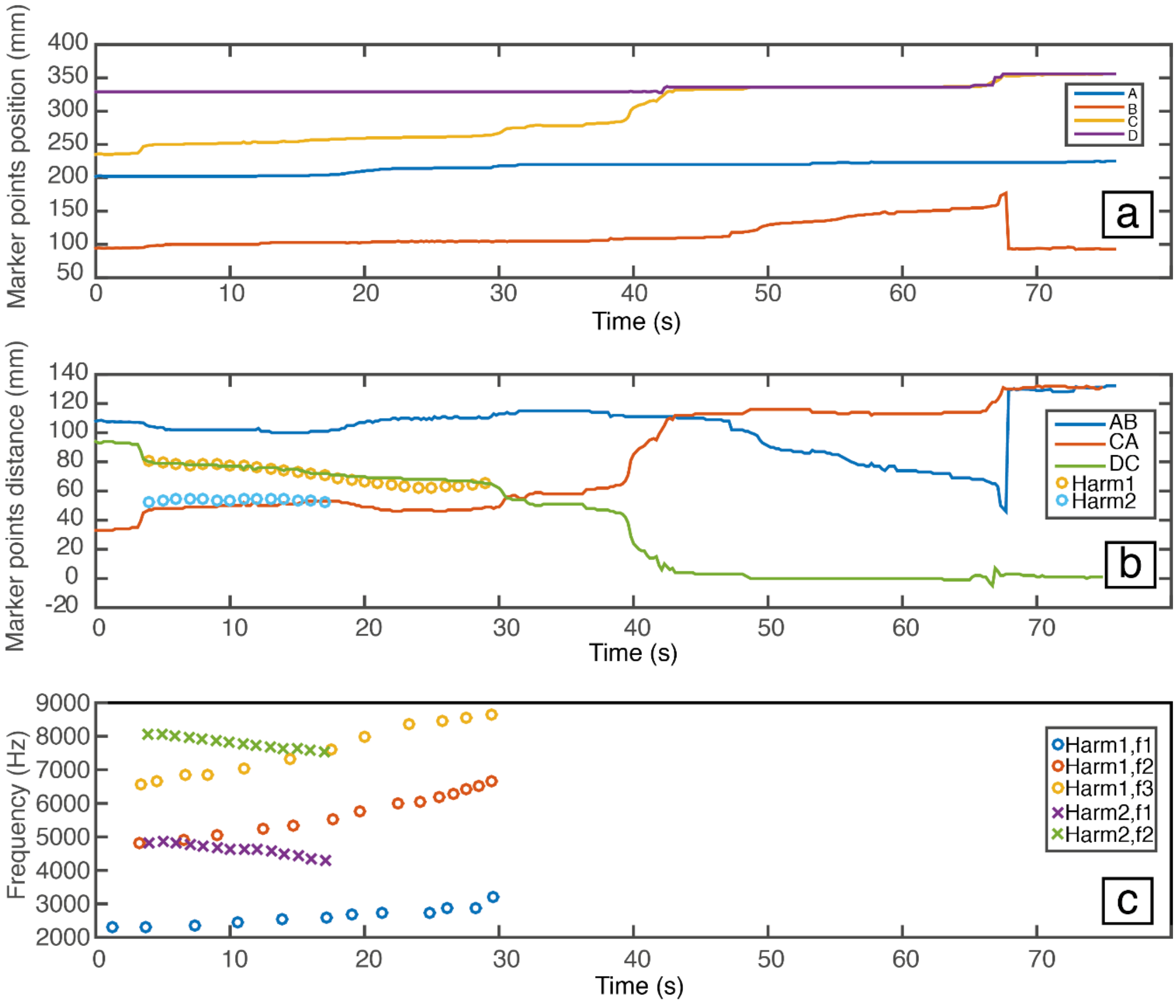

Figure 4*: (a) Temporal evolution of gas pockets through video images. The experimental conditions are: viscosity 1,000 Pa s, gas flux 120x10^{-3} l/s, conduit roughness C1 (run 312). From the lowest to the highest gas pocket at time zero: B (orange line), A (blue line), C (yellow line), D (purple line). The distance of each point is taken with reference to the conduit base. (b) Length of gas pockets AB (blue line), CA (red line), DC (green line). Yellow and azure dots represent the modelled length of the resonator for the group of primary harmonics (Harm1) with positive trend and for the secondary harmonics (Harm2) with negative envelope. (c) Frequency values of different spectral lines (colored dots) of the principal group of harmonics and of secondary harmonics (colored crosses).*

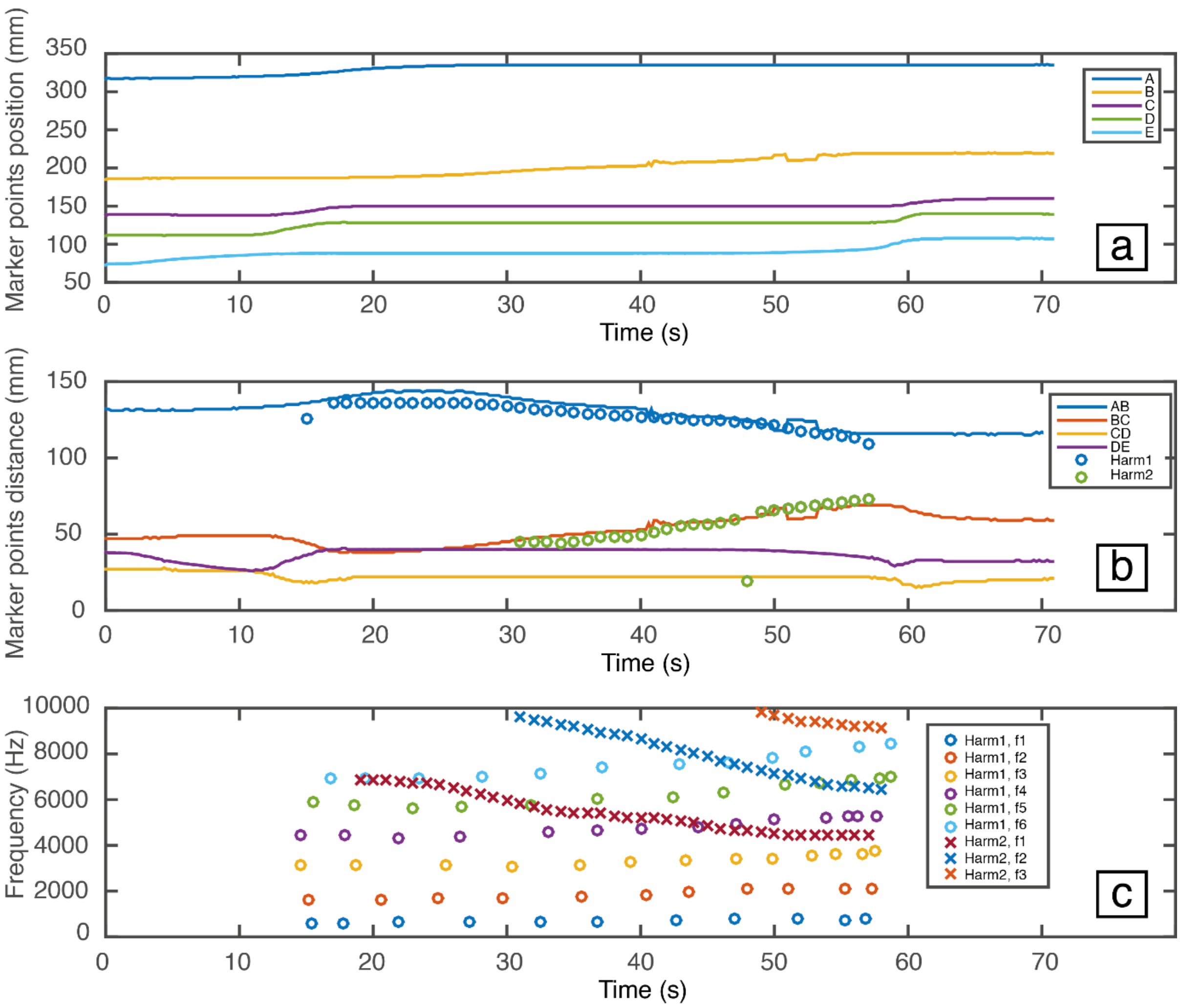

***Figure 5**: (a) Temporal evolution of gas pockets through video images. The experimental conditions are: viscosity 1,000 Pa s, gas flux 180x10^{-3} l/s, conduit roughness C1 (run 353). From the lowest to the highest gas pocket at time zero: E (azure line), D (green line), C (purple line), B (yellow line), A (blue line). The distance of each point is taken with reference to the conduit base. (b) Length of gas pockets AB (blue line), BC (red line), CD (yellow line), DE (purple line). Blue and green dots represent the modelled length of the resonator for the group of primary harmonics (Harm1) with positive trend and for the secondary harmonics (Harm2) with negative envelope. (c) Frequency values of different spectral lines (f1, f2, etc.) of the principal group of harmonics (colored dots) and of secondary harmonics (colored crosses).*

Among the different models suggested to explain harmonic tremor and the associated gliding phenomena, cited in **Section 1**, we tested whether a model of resonance of the gas pockets could justify the frequency values, as well as their temporal variations, observed in the spectrograms of both accelerometric and acoustic signals. In particular, since such gas pockets have a roughly cylindrical shape, we took into account a simple pipe-like resonator model. In the case of closed–closed gas pocket, we expect to observe $n\lambda/2$ (λ = wavelength, n=1,2,3,...) waves as longitudinal resonance modes, while, if one end is open and the other closed, $(2n-1)\lambda/4$ waves should be observed (e.g. De Angelis and McNutt, 2007). The closed ends of the gas pockets can be considered as the constrictions connecting contiguous units. Hence, the set of frequencies *f* characterizing the resonance-generated harmonics will be (Kobayashi et al., 2010, and references therein):

$$f = nv/(2L) \qquad \text{with } n=1,2,3,\ldots \tag{1}$$

$$f = nv/(4L) \qquad \text{with } n=1,3,5,\ldots \tag{2}$$

in the case of closed–closed and closed-open churn units, respectively. The term *v* indicates the acoustic velocity of the air filling the churn unit, and *L* the length of the gas pockets. By these equations, a relationship linking the resonator length with the frequency spacing between consecutive harmonics (Δf) can be obtained:

$$L = v/(2 * \Delta f) \tag{3}$$

valid for both closed–closed and closed-open systems. As it was difficult to reconstruct the whole set of harmonics composing the observed gliding especially at low frequencies, equation (3) was used in place of equations (1) and (2) to constrain the theoretical lengths of the resonating gas pockets. The theoretical average length of the resonator at a given time, computed following the procedure detailed in **Section 2** and using **equation (3)** is plotted in **Figures 4** and **5** (panel b) and **Supplementary Figures 1** to **6** as colored dots to verify whether such a resonating model is able to justify the observed gliding phenomena.

In case of a closed-open system and pipe width relatively large with respect to the length, the end effects should be considered. In that case, the effective pipe length, determining the resonance frequencies, is given by (Johnson et al., 2018 and references therein):

$$L_{eff} = L + \Delta L = L + 8a / (3\pi) \tag{4}$$

where *a* is the gas pocket radius. Considering a radius of 1.5 cm and assuming a gas pocket length ranging from 5 to 20 cm, neglecting the open-end correction in equation (3) leads to an overestimation of the resonating churn unit length equal to 25 - 6%, respectively.

4. Discussion

Here we present the first study of seismo-acoustic harmonic gliding tremor generated during laboratory experiments. Harmonic tremor has been widely generated in our experimental dataset, the clearest and most stable examples being related to high viscosities and/or high flux rate conditions. Gliding of harmonic spectral lines of the seismic and acoustic tremor has been observed exclusively in the churn/annular-like flow regime, as shown in **Figure 3**. These observations suggest a relevant role of the degassing pattern, hence of the spatial distribution of gas and liquid phases, at the onset of harmonic tremor and on its gradual shift over time in our experiments. Churn flow is defined as an intermediate flow regime occurring in between slug and annular flow patterns and characterized by local flooding (i.e. the liquid is carried upward by the gas phase, e.g. Pioli et al., 2012, and references therein). During churn flow the gas-liquid travels upward and downward in a churning or oscillating movement with a resultant of upward flow (e.g. Mohammed et al., 2018 and references therein).

Whilst the majority of studies have addressed churn and annular regimes using low viscous fluids, such as water or fluids with similar properties (e.g. Shah et al., 1982), only recently Mohammed et al. (2018; 2019) and Hasan et al. (2019) investigated churn flow in a high viscosity system and large-pipe diameter (240 and 290 mm) using 330 and 360 Pa s silicone oils. They identify the transition from slug to churn flow regime at a gas superficial velocity (that is the ratio between gas volume flux and pipe cross-sectional area) of 0.127-0.108 m/s, the effective fully developed churn flow being observed at higher superficial velocities of 0.336-0.566 m/s, similarly to Pioli et al. (2012). In our study, the range of superficial velocities of 0.04-0.25 m/s (where gliding episodes were observed) included mostly the disruption of slug flow and the so-called “transition to churn flow” (Mohammed et al., 2018, 2019) and churn flow episodes with few observations of annular sustained flow. The discrepancies between different setups are not surprising as transition between various regimes depends not only on the liquid and gas properties but also on the geometrical aspect of the conduit and on the distributor design, and scaling of highly complex and nonlinear two-phase behavior is a highly complex task (Urseanu, 2000; Mohammed et al., 2019).

According to Mohammed et al. (2018), regions of high frequency of the void fraction, likely due to liquid bridges flowing up and down, appear upon reaching the above-mentioned threshold for the transition to churn flow: indeed, the increasing gas flux forces coalescence between consecutive elongated Taylor bubbles, that progressively lose their round shape. The liquid slugs between bubbles progressively disappear and are replaced by churn areas that are initially connected to Taylor bubbles by small necks. As the gas flow rate increases, a more complicated gas pattern appears, progressively replacing elongated slugs. We hypothesized here that the observed small over-pressurized gas pockets connected by thin necks and quite unstable, have a primary role in the generation of gliding tremor patterns. Interestingly, Mohammed et al. (2018) reported similarity between the sound produced by air passing through high viscosity liquids during their experiments and acoustic signals from Arenal volcano in Costa Rica.

The generation of open and stable degassing pathways has been related to the observation of harmonic acoustic signals by Lyons et al. (2013). The authors performed a set of degassing experiments generating a harmonic signal by the flow of compressed air through a valve, located below a tank of viscoelastic analogue magma. Clear harmonic oscillation and the transmission of the signal to the atmosphere was observed only for high stiffness fluids, featuring open stable degassing pathways (Lyons et al., 2013). Accordingly, we believe that the spatial distribution of the gas phase and the efficiency of its coupling with the atmosphere plays an important role on the characteristics of the observed seismo-acoustic tremor.

Based on this evidence, we assumed that gas pockets observed in a churn -like regime resonate as a pipe-like resonator, and that their unstable dynamics might be responsible for the observed episodes of tremor gliding. The theoretical lengths of the pipe-like resonators, constrained by **equation (3)**, matched quite well with the observed lengths of the gas pockets in six cases out of eight (**Figures 4** and **5** and **Supplementary Figures 1** to **6**), suggesting how such a simple resonance model is able to explain the recorded gliding phenomena. Similar to the model suggested by Lesage et al. (2006), the resonance is likely to be triggered by the air escaping through the churn unit constrictions. In two other cases, particularly low Δf values led to model long resonating pipes, which did not coincide with any gas pocket, but rather with the conduit portion above the upper constriction (**Supplementary Figures 2 and 5**). In accordance with this, previous laboratory studies have highlighted how the length of a pipe portion open to the atmosphere determines the resonance frequencies observed in the acoustic signals and might be triggered by the bursting taking place inside the pipe (Vidal et al., 2006). In addition, it is particularly noteworthy that, even in cases when a double set of harmonics with opposite patterns (increasing and decreasing frequencies with time) is observed, the pipe-like churn resonator allowed modelling the observed antithetical length changes of two contiguous gas pockets (**Figures 4** and **5**). Remarkably, both decreasing gliding episodes and the occurrence of different sets of spectral peaks with independent gliding behavior, as here observed, were reported by Lesage et al. (2006) for Arenal Volcano (Costa Rica). They invoke gas valve leaking caused by progressive pressure decrease as the source of negative tremor gliding, similar to our experimental observations. In some cases, gliding with increasing frequency pattern was observed preceding transients with higher amplitude, recorded in both accelerometric and acoustic signals. This evidence matches well with gliding phenomena observed before explosions on some volcanoes such as Arenal (Lesage et al., 2006), Soufrière Hills (Powell and Neuberg, 2003) and Redoubt (Hotovec et al., 2013). In our experiments, the higher amplitude transients observed in both accelerometric and acoustic signals are accompanied by a quick upward migration of a gas pocket constriction and an explosive release of gas. Hence, the phenomena that are likely to lead to such “explosions” are: i) gradual closing of a constriction due to the downward flooding of the falling liquid film above; ii) increase of pressure exerted by the gas on the constriction and slow upward migration of this constriction; iii) once a given pressure threshold is reached, the upward migration of the constriction accelerates and the elastic energy release increases. The (ii) and (iii) phenomena are accompanied by gliding with a main increasing frequency pattern (slow and fast in case of (ii) and (iii) respectively), testifying the length decrease of the churn unit located above the constriction.

Churn flow has been hypothesized to occur in violent Strombolian up to lava fountain activities (e.g. Pioli et al., 2008; Ulivieri et al., 2013). At Paricutin volcano, Pioli et al. (2008) suggested that the transition between Strombolian and violent Strombolian (cineritic) eruption reflects the transition between slug and churn flow resulting from differences in gas accumulation within the cone. Ulivieri et al. (2013) assumed that the monochromatic acoustic signal recorded during oscillation of the eruptive column during several episodes of fire fountaining at Mt. Etna are related to the churn flow degassing regime. According to Fowler and Robinson (2018), the churn-turbulent regime is expected for low viscosity basalts in wide conduits above a critical volume fraction threshold that depends also upon magma properties and its ability to foam. Hence, the occurrence of mild Strombolian explosions and more violent gas-and-ash-rich explosions are indicative of slug/churn annular flow, the latter being more plausible for wide conduit (Fowler and Robinson, 2018).

A comparison between natural system and experimental observations requires to account for the balance of the different forces acting on the two-phase systems. To this aim, we used the Buckingham Π Theorem (e.g. Brand, 1957) to define the relevant a-dimensional groups for the following physical variables characterizing the experiments: η liquid viscosity, ρ_l liquid density, D conduit diameter, U_{gas} gas superficial velocity, D_{churn} churn diameter, σ surface tension. We obtained three a-dimensional Π groups

$$\Pi_1 = \frac{u_{gas}\eta}{\sigma} \quad (5)$$

$$\Pi_2 = \frac{\rho_l \sigma D}{\eta^2} \quad (6)$$

$$\Pi_3 = \frac{D_{churn}}{D} \quad (7)$$

Π_2 is equivalent to Oh^{-2}, where Oh stands for the Ohnesorge number, a dimensionless number commonly use to relate viscous to inertial and surface tension forces whereas Π_3 is a dimensionless gas pocket diameter. The comparison of the Π groups computed for natural basaltic systems, for our experiments and for high-viscous churn flow studies is shown in **Table 1**. For the range of superficial velocities (0.04-0.25 m/s) and viscosities (100 and 1,000 Pa s) characterizing the degassing regimes exhibiting acoustic and/or seismic gliding, a Π_1 on the order of 10^2-10^4 was observed, similarly to Hasan et al. (2019). For basaltic volcanoes, assuming a viscosity in the range 10^2-10^3 Pa s and a surface tension of 0.3 N/m, a value of Π_1 on the order of 10^2-10^4 would be compatible with a surface velocity of 0.5-5 m/s, that implies a flux rate of 10^2-10^3 m^3/s (e.g. Ishii et al., 2019) for a conduit with diameter of 15 m. A value of Π_3 of 0.5-0.9 is compatible with an experimental churn diameter of 1.5-2.7 cm and for a volcanic conduit of 15 m corresponds to a volcanic churn dimension of 2-14 m. A major discrepancy is found when comparing Π_2 for experimental system and for volcanoes, natural system having a Π_2 of several order of magnitude higher than experimental ones. As a result, we expect inertial forces to have a much relevant role on gravitational and surface forces in our experimental system compared to volcanoes. The Π numbers were complemented by the Morton Number to account for the role of buoyancy, defined as

$$M_0 = \frac{g\eta^4\Delta\rho}{\rho_l{}^2\sigma^3} \tag{8}$$

Where $\Delta\rho$ is the density difference between the gas and liquid phases and *g* represent the gravitational acceleration. In our experiments, the Morton number has values of 10^{11}-10^{15}, at the higher range of the expected Morton Number for Strombolian activity at volcano scale condition (Del Bello et al. 2012). Furthermore, we computed the Reynold Number of the two-phase-flow in the churn-annular regime after Seyfriend and Freund (2000) assuming a volume liquid percentage of 20% of the total along a hypothetical section of the conduit, at 1-5 bar and for a density of compressed air of 1.18-5.94 kg/m3 we obtain values on the order of 10^{-2}-10^{-3}. Such low Reynold Numbers are typical of experiments performed with high viscous liquids (Hasan et al. 2019) and fits the hypothesized values for weak explosive activity at basaltic volcanoes (e.g. La Spina et al. 2021) and the hypothesis of a laminar regime before the onset of fragmentation (Lane et al. 2001).

Finally, it is worth noting that even though the scale of pipe resonance is clearly different in volcanoes and laboratory environments, they comply with a simple size (*d*) - frequency (*f*) scaling law (Burlini et al., 2007; Benson et al., 2008; Fazio et al., 2019). In fact, assuming a fundamental frequency for experimental churn resonance in the range 500-7000 Hz and a length of the churn of 3-30 cm, a simple size-frequency scaling law would suggest a length of volcanic churns to be in the range of 8-200 m for resonator fundamentals of 0.5-10 Hz. The length of the churn for volcanic environments fits with previous values theorized for volcanic slugs during Strombolian to fire fountain activities (e.g. 8-100 m, Vergniolle and Ripepe, 2008; 13-120 m, Kremers et al., 2013; 76-260 m, Ilanko et al., 2020).

However, despite the clear importance of the churn regime for unveiling the dynamics of the spectrum of eruptive styles in between violent Strombolian and fire fountain eruptions, studies addressing the dynamics of volcanic churn flow in volcanoes are few. We strongly recommend that future studies will fill this gap and contribute to define the characteristics of the volcanic churn regime. One of the key point for future research lies in the conduit geometry, meaning conduit diameter and length. Provided as we did here that conduit roughness has no influence on the source of gliding (although it does affect harmonic tremor; Spina et al., 2019), future studies performed possibly using a range of higher diameter and length of the experimental conduit will have the double advantage of ensuring stable conditions of the degassing flow and provide further constraints for the source of low frequency hindering the fundamental of harmonic tremor. In fact, longer conduits would minimize the contribution of gas injection on acoustic and seismic sensors distributed along the conduit, and offer the possibility to explore different conduit resonance modes, both possibly affecting the low frequency band (roughly <2000 Hz) where the fundamental of harmonic tremor lies. Further improvements on the sensor system would possibly help gain much information on harmonic tremor during churn flow, such as: 1) deploying a higher number of accelerometer or 2) using an ECT (Electrical Capacitance Tomography) probe to reconstruct the internal distribution of the liquid phase (including film thickness and its possible flooding waves).

5. Concluding remarks

We present here the first experimental set of laboratory studies mimicking the temporal migration of the spectral lines of harmonic tremor, i.e. gliding, observed during analogue degassing experiments. The results are summarized in bullet points below.

1. Gliding of the harmonic acoustic and seismic tremor has been observed in intermediate-high viscosity experiments (100-1,000 Pa s) for degassing regimes mainly corresponding to transition to churn-like flow and churn-like flow. It was associated mostly but not exclusively with an increasing trend of the gliding spectral lines. In a few cases, two sets of gliding harmonics were observed, with the secondary set of harmonics exhibiting a decreasing trend. Positive gliding preceding high amplitude transients has often been observed.
2. We particularly selected from our dataset eight episodes of gliding that were outstanding for clarity of the harmonic gliding signals. On such experimental runs, spectral analyses performed on the acoustic signal were compared against a quantitative tracking of the length of churn areas.
3. The evolution of the theoretical length of the churn resonator, derived from the spacing between consecutive harmonics, matches very closely with the variation of the length of the most superficial gas pocket in up to six cases. All the same, the secondary set of negative harmonics, if present, suggests a resonator length that closely resembles the second to last gas pocket. The remaining cases provide a match for the theoretical resonator length with the length of the upper portion of the experimental conduit above the highest liquid constriction, as previously already known in literature.
4. Experimental evidence suggests that gliding harmonic tremor might result from the progressive length variation of interconnected over-pressurized gas pockets that characterize churn/annular-like degassing regime.

Acknowledgments

We wish to thank the Editor, Chiara Petrone and the two reviewers John Lyons and Laura Pioli for their careful review of this paper. L.S. wish to thank the bottom up project "ROUGHER" funded by INGV and INGV Departmental Strategic Project UNO (UNderstanding the Ordinary to forecast the extraordinary: An integrated approach for studying and interpreting the explosive activity at Stromboli volcano).A.C. thanks CHANCE project, II Edition, Università degli Studi di Catania (principal investigator A. Cannata) and grant PIACERI, 2020-22 programme (PAROSSISMA project, code 22722132140; principal investigator Marco Viccaro). DM acknowledges the MIUR project n. PRIN2017-2017LMNLAW "Connect4Carbon".

References

Almendros, J., Abella, R., Mora, M., & Lesage, P. (2012). Time-Dependent Spatial Amplitude Patterns of Harmonic Tremor at Arenal Volcano, Costa Rica: Seismic-Wave Interferences?. Bulletin of the Seismological Society of America, 102(6), 2378-2391.

Arciniega-Ceballos, A., Alatorre-Ibargüengoitia, M., Scheu, B., Dingwell, D. B., & Delgado-Granados, H. (2014). Seismological analysis of conduit dynamics in fragmentation experiments. *Journal of Geophysical Research: Solid Earth*, *119*(3), 2215-2229.

Benson, P. M., Vinciguerra, S., Meredith, P. G., & Young, R. P. (2008). Laboratory simulation of volcano seismicity. *Science*, *322*(5899), 249-252.

Burlini, L., Vinciguerra, S., Di Toro, G., De Natale, G., Meredith, P., & Burg, J. P. (2007). Seismicity preceding volcanic eruptions: New experimental insights. *Geology*, *35*(2), 183-186.

Brand, L. (1957). The Pi theorem of dimensional analysis. Archive for Rational Mechanics and Analysis, 1(1), 35-45.

Chouet, B., (1985). Excitation of a buried magmatic pipe: a seismic source model for volcanic tremor. Journal of Geophysical Research 90, 1881–1893.

Clarke, J., Adam, L., Sarout, J., van Wijk, K., Kennedy, B., & Dautriat, J. (2019). The relation between viscosity and acoustic emissions as a laboratory analogue for volcano seismicity. Geology, 47(6), 499-503.

De Angelis, S., & McNutt, S.R. (2007). Observations of volcanic tremor during the January–February 2005 eruption of Mt. Veniaminof, Alaska. Bulletin of Volcanology 69.8: 927-940.

Del Bello, E., Llewellin, E. W., Taddeucci, J., Scarlato, P., & Lane, S. J. (2012). An analytical model for gas overpressure in slug-driven explosions: Insights into Strombolian volcanic eruptions. *Journal of Geophysical Research: Solid Earth*, *117*(B2).

Fazio, M., Alparone, S., Benson, P. M., Cannata, A., & Vinciguerra, S. (2019). Genesis and mechanisms controlling tornillo seismo-volcanic events in volcanic areas. *Scientific reports*, *9*(1), 1-11.

Fowler, A. C., & Robinson, M. (2018). Counter-current convection in a volcanic conduit. *Journal of Volcanology and Geothermal Research*, *356*, 141-162.

Giudicepietro, F., Esposito, A. M., Spina, L., Cannata, A., Morgavi, D., Layer, L., & Macedonio, G. (2020). Clustering of experimental seismo-acoustic events using Self-Organizing Map (SOM). Frontiers in Earth Science, 8, 723.

Hagerty, M. T., Schwartz, S. Y., Garces, M. A., & Protti, M. (2000). Analysis of seismic and acoustic observations at Arenal Volcano, Costa Rica, 1995–1997. Journal of Volcanology and Geothermal Research, 101(1-2), 27-65.

Hasan, A. H., Mohammed, S. K., Pioli, L., Hewakandamby, B. N., & Azzopardi, B. J. (2019). Gas rising through a large diameter column of very viscous liquid: Flow patterns and their dynamic characteristics. International Journal of Multiphase Flow, 116, 1-14.

Hellweg, M., (2000). Physical models for the source of Lascar's harmonic tremor. Journal of Volcanology and Geothermal Research 101, 183–198.

Hewitt, G. F. (1985). Experimental and modelling studies of annular flow in the region between flow reversal and the pressure drop minimum. Physico-Chemical Hydrodynamics, 6, 43-50.

Hotovec, A. J., Prejean, S. G., Vidale, J. E., & Gomberg, J. (2013). Strongly gliding harmonic tremor during the 2009 eruption of Redoubt Volcano. Journal of Volcanology and Geothermal Research, 259, 89-99.

James, M. R., Lane, S. J., Chouet, B., & Gilbert, J. S. (2004). Pressure changes associated with the ascent and bursting of gas slugs in liquid-filled vertical and inclined conduits. *Journal of Volcanology and Geothermal Research*, *129*(1-3), 61-82.

Jellinek, A.M., & Bercovici, D., (2011). Seismic tremors and magma wagging during explosive volcanism. Nature 470, 522–525.

Johnson, J. B., & Lees, J. M. (2000). Plugs and chugs—seismic and acoustic observations of degassing explosions at Karymsky, Russia and Sangay, Ecuador. Journal of Volcanology and Geothermal Research, 101(1-2), 67-82.

Johnson, J. B., Ruiz, M. C., Ortiz, H. D., Watson, L. M., Viracucha, G., Ramon, P., & Almeida, M. (2018). Infrasound tornillos produced by Volcán Cotopaxi’s deep crater. Geophysical Research Letters, 45, 5436–5444. https://doi.org/10.1029/2018GL077766.

Kobayashi, T., Namiki, A., & Sumita, I. (2010). Excitation of airwaves caused by bubble bursting in a cylindrical conduit: Experiments and a model. Journal of Geophysical Research: Solid Earth, 115(B10).

Kremers, S., Wassermann, J., Meier, K., Pelties, C., van Driel, M., Vasseur, J., & Hort, M. (2013). Inverting the source mechanism of Strombolian explosions at Mt. Yasur, Vanuatu, using a multi-parameter dataset. *Journal of volcanology and geothermal research*, *262*, 104-122.

Ichihara, M., Lyons, J. J., & Yokoo, A. (2013). Switching from seismic to seismo-acoustic harmonic tremor at a transition of eruptive activity during the Shinmoe-dake 2011 eruption. Earth, Planets and Space, 65(6), 633-643.

Ilanko, T., Pering, T. D., Wilkes, T. C., Woitischek, J., D'Aleo, R., Aiuppa, A., ... & Garaebiti, E. (2020). Ultraviolet Camera Measurements of Passive and Explosive (Strombolian) Sulphur Dioxide Emissions at Yasur Volcano, Vanuatu. *Remote Sensing*, *12*(17), 2703.

Ishii, K., Yokoo, A., Kagiyama, T., Ohkura, T., Yoshikawa, S., & Inoue, H. (2019). Gas flow dynamics in the conduit of Strombolian explosions inferred from seismo-acoustic observations at Aso volcano, Japan. Earth, Planets and Space, 71(1), 1-15.

La Spina, G., Arzilli, F., Llewellin, E. W., Burton, M. R., Clarke, A. B., Vitturi, M. D. M., ... & Mader, H. M. (2021). Explosivity of basaltic lava fountains is controlled by magma rheology, ascent rate and outgassing. Earth and Planetary Science Letters, 553, 116658.

Lane, S. J., Chouet, B. A., Phillips, J. C., Dawson, P., Ryan, G. A., & Hurst, E. (2001). Experimental observations of pressure oscillations and flow regimes in an analogue volcanic system. *Journal of Geophysical Research: Solid Earth*, *106*(B4), 6461-6476.

Lees, J. M., Johnson, J. B., Ruiz, M., Troncoso, L., & Welsh, M. (2008). Reventador Volcano 2005: Eruptive activity inferred from seismo-acoustic observation. Journal of Volcanology and Geothermal Research, 176(1), 179-190.

Lees, J. M., & Ruiz, M. (2008). Non-linear explosion tremor at Sangay, Volcano, Ecuador. Journal of Volcanology and Geothermal Research, 176(1), 170-178.

Lesage, P., Mora,M.M., Alvarado, G.E., Pacheco, J., & Métaxian, J. (2006). Complex behavior and source model of the tremor at Arenal volcano, Costa Rica. Journal of Volcanology and Geothermal Research 157, 49–59.

Lyons, J. J., Ichihara, M., Kurokawa, A., & Lees, J. M. (2013). Switching between seismic and seismo-acoustic harmonic tremor simulated in the laboratory: Insights into the role of open degassing channels and magma viscosity. Journal of Geophysical Research: Solid Earth, 118(1), 277-289.

McNutt, S. R., & Nishimura, T. (2008). Volcanic tremor during eruptions: temporal characteristics, scaling and constraints on conduit size and processes. Journal of Volcanology and Geothermal Research, 178(1), 10-18.

McNutt, S. R., & Roman, D. C. (2015). Volcanic seismicity. In The Encyclopedia of Volcanoes (pp. 1011-1034). Academic Press.

Mohammed, S. K., Hasan, A., Dimitrakis, G., & Azzopardi, B. J. (2018). Churn flow in high viscosity oils and large diameter columns. International Journal of Multiphase Flow, 100, 16-29.

Mohammed, S. K., Hasan, A. H., Ibrahim, A., Dimitrakis, G., & Azzopardi, B. J. (2019). Dynamics of flow transitions from bubbly to churn flow in high viscosity oils and large diameter columns. International Journal of Multiphase Flow, 120, 103095.

Neuberg, J., Luckett, R., Baptie, B., & Olsen, K. (2000). Models of tremor and low-frequency earthquake swarms on Montserrat. Journal of Volcanology and Geothermal Research, 101(1-2), 83-104.

Pering, T. D., & McGonigle, A. J. (2018). Combining spherical-cap and Taylor bubble fluid dynamics with plume measurements to characterize basaltic degassing. Geosciences, 8(2), 42.

Pioli, L., Erlund, E., Johnson, E., Cashman, K., Wallace, P., Rosi, M., & Granados, H. D. (2008). Explosive dynamics of violent Strombolian eruptions: the eruption of Parícutin Volcano 1943–1952 (Mexico). Earth and Planetary Science Letters, 271(1-4), 359-368.

Pioli, L., Bonadonna, C., Azzopardi, B. J., Phillips, J. C., & Ripepe, A. M. (2012). Experimental constraints on the outgassing dynamics of basaltic magmas. Journal of Geophysical Research: Solid Earth, 117(B3).

Powell, T. W., & Neuberg, J. (2003). Time dependent features in tremor spectra. Journal of Volcanology and Geothermal Research, 128(1-3), 177-185.

Ripepe, M., Delle Donne, D., Lacanna, G., Marchetti, E., & Ulivieri, G. (2009). The onset of the 2007 Stromboli effusive eruption recorded by an integrated geophysical network. Journal of Volcanology and Geothermal Research, 182(3-4), 131-136.

Rowe, C. A., Aster, R. C., Kyle, P. R., Dibble, R. R., & Schlue, J. W. (2000). Seismic and acoustic observations at Mount Erebus volcano, Ross island, Antarctica, 1994–1998. Journal of Volcanology and Geothermal Research, 101(1-2), 105-128.

Seyfried, R., & Freundt, A. (2000). Experiments on conduit flow and eruption behavior of basaltic volcanic eruptions. Journal of Geophysical Research: Solid Earth, 105(B10), 23727-23740.

Schlindwein, V., Wassermann, J., & Scherbaum, F. (1995). Spectral analysis of harmonic tremor signals at Mt. Semeru volcano, Indonesia. Geophysical research letters, 22(13), 1685-1688.

Shah, Y. T., Kelkar, B. G., Godbole, S. P., & Deckwer, W. D. (1982). Design parameters estimations for bubble column reactors. *AIChE Journal*, *28*(3), 353-379.

Spina, L., Morgavi, D., Cannata, A., Campeggi, C., & Perugini, D. (2018). An experimental device for characterising degassing processes and related elastic fingerprints: analogue volcano seismo-acoustic observations. Review of Scientific Instruments, 89, 055102, doi: 10.1063/1.5020004.

Spina, L., Cannata, A., Morgavi, D., & Perugini, D. (2019). Degassing behaviour at basaltic volcanoes: New insights from experimental investigations of different conduit geometry and magma viscosity. Earth Science Review, https://doi.org/10.1016/j.earscirev.2019.03.010.

Ulivieri, G., Ripepe, M., & Marchetti, E. (2013). Infrasound reveals transition to oscillatory discharge regime during lava fountaining: Implication for early warning. Geophysical Research Letters, 40(12), 3008-3013.

Urseanu,M. (2000). Scaling Up Bubble Column Reactors (Ph.D.thesis). Universityof Amsterdam, Amsterdam,Netherlands.

Vergniolle, S., & Jaupart, C. (1986). Separated two-phase flow and basaltic eruptions. Journal of Geophysical Research: Solid Earth, 91(B12), 12842-12860.Vergniolle, S, & Ripepe, M. (2008). From Strombolian explosions to fire fountains at Etna Volcano (Italy): what do we learn from acoustic measurements?. *Geological Society, London, Special Publications*, *307*(1), 103-124.

Vergniolle, S., & Ripepe, M. (2008). From Strombolian explosions to fire fountains at Etna Volcano (Italy): what do we learn from acoustic measurements?. Geological Society, London, Special Publications, 307(1), 103-124.

Vidal, V., Géminard, J. C., Divoux, T., & Melo, F. (2006). Acoustic signal associated with the bursting of a soap film which initially closes an overpressurized cavity. The European Physical Journal B-Condensed Matter and Complex Systems, 54(3), 321-339.

Supplementary Figures

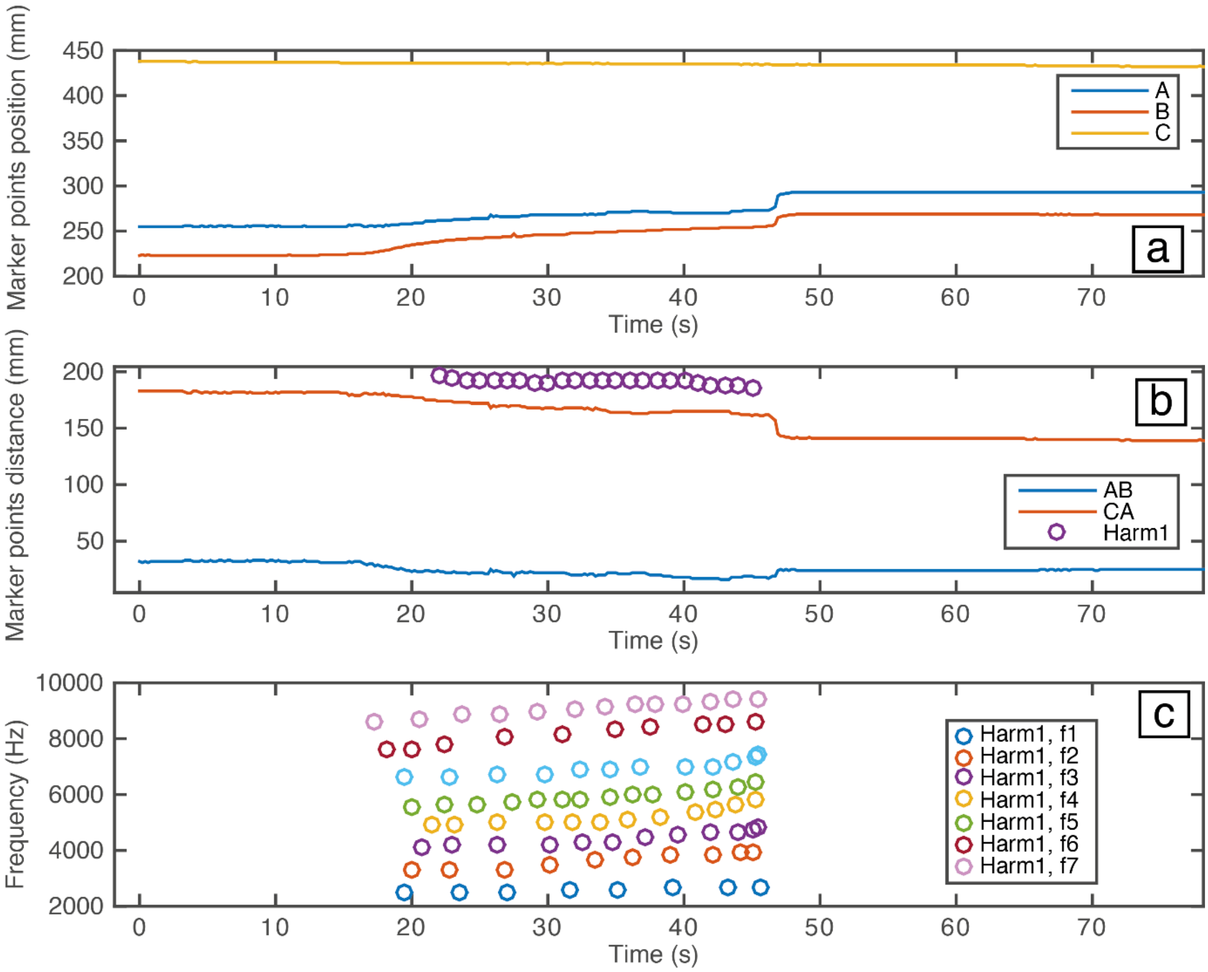

***Supplementary Figure 1**: (a) Temporal evolution of gas pockets through video images. The experimental conditions are: viscosity 1,000 Pa s, gas flux 180x10^{-3} l/s, conduit roughness C2 (run 309). From the lowest to the highest gas pocket unit at time zero: B (orange line), A (blue line), C (yellow line). The distance of each point is taken with reference to the conduit base. (b) Length of gas pocket units AB (blue line), CA (red line). Purple dots represent the modelled length of the resonator for harmonics (Harm1) shown in (c). (c) Frequency values of different spectral lines (f1, f2, etc.) of the principal group of harmonics (colored dots).*

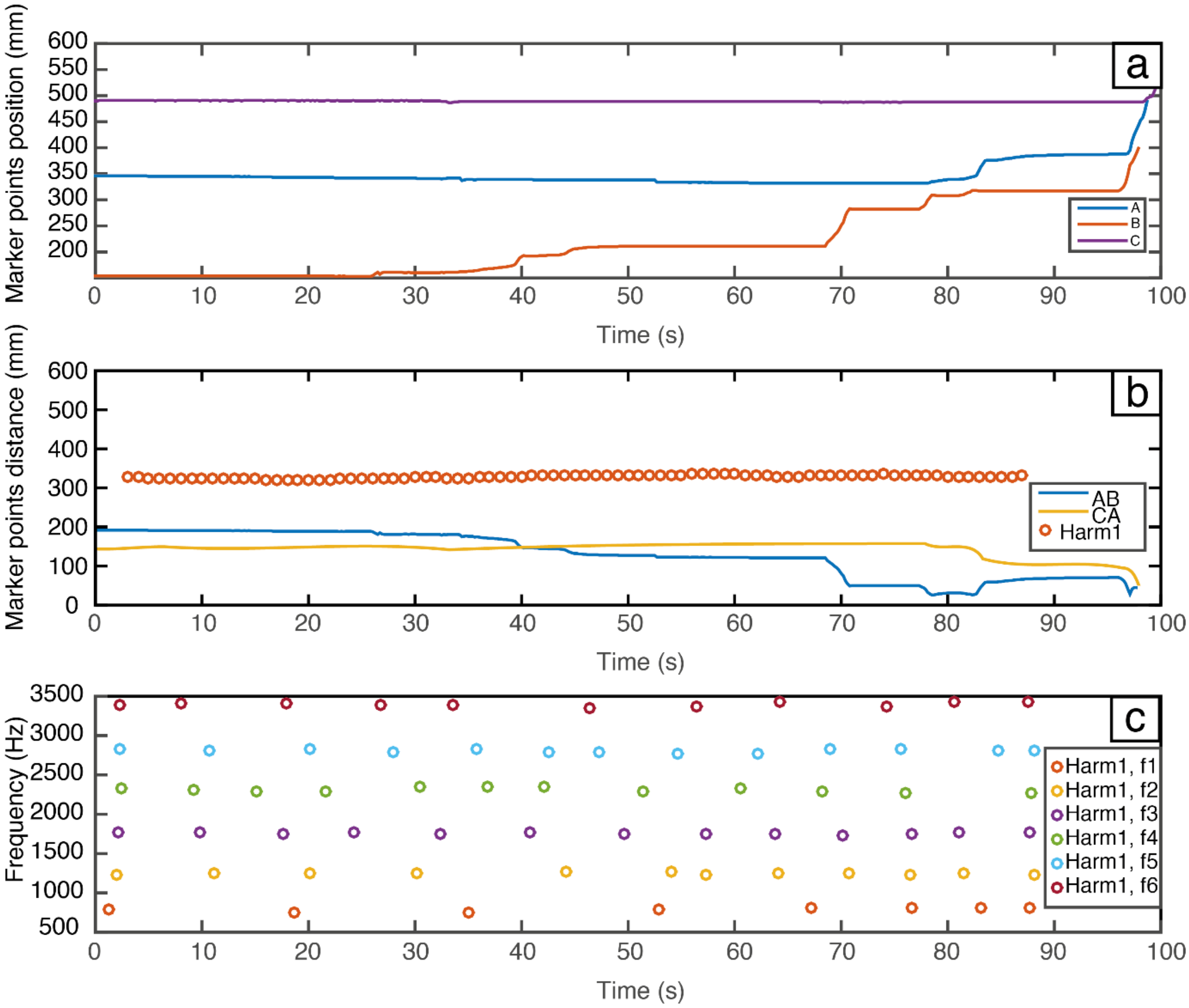

***Supplementary Figure 2**: (a) Temporal evolution of gas pocket units through video images. The experimental conditions are: viscosity 1,000 Pa s, gas flux 30x10^{-3} l/s, conduit roughness C2 (run 324). From the lowest to the highest gas pocket unit at time zero: B (orange line), A (blue line), C (purple line). The distance of each point is taken with reference to the conduit base. (b) Length of gas pocket units AB (blue line), CA (red line). Orange dots represent the modelled length of the resonator for harmonics shown in (c). (c) Frequency values of different spectral lines (f1, f2, etc.) of the principal group of harmonics (colored dots). Note that the open conduit core above gas pockets termination C up to the conduit surface has a rather stable length of ca. 330 cm.*

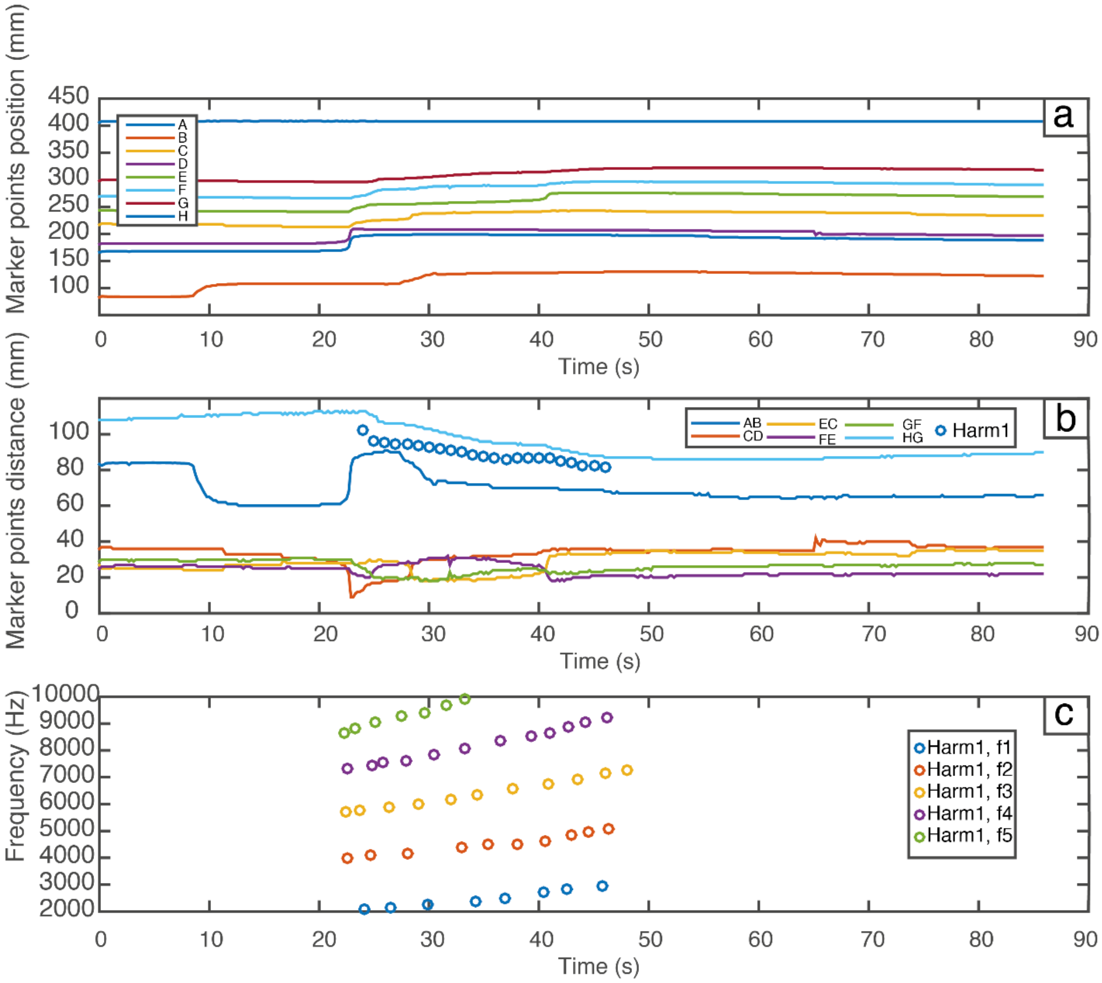

Supplementary Figure 3*: (a) Temporal evolution of gas pocket units through video images. The experimental conditions are: viscosity 1,000 Pa s, gas flux $120x10^{-3}$ l/s, conduit roughness C1 (run 361). From the lowest to the highest gas pocket unit at time zero: B (orange line), A (blue line), D (purple line), C (yellow line), E (green line), F (azure line), G (brown line), H (light blue line). The distance of each point is taken with reference to the conduit base. (b) Length of gas pocket units AB (blue line), CD (red line), EC (yellow line), FE (purple line), GF (green line), HG (azure line). Blue dots represent the modelled length of the resonator for harmonics shown in (c). (c) Frequency values of different spectral lines (f1, f2, etc.) of the principal group of harmonics (colored dots).*

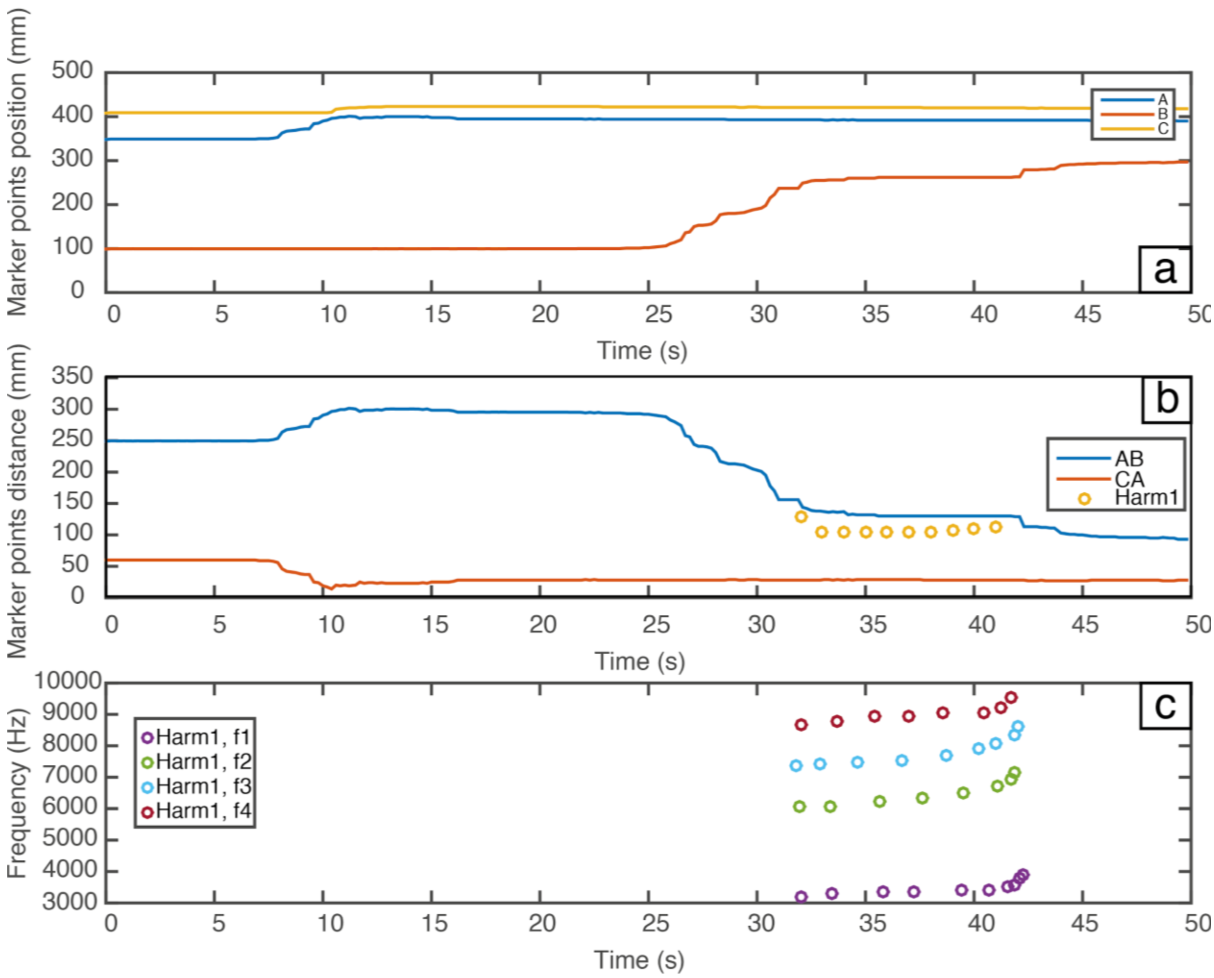

Supplementary Figure 4*: (a) Temporal evolution of gas pocket units through video images. The experimental conditions are: viscosity 1,000 Pa s, gas flux 90x10^{-3} l/s, conduit roughness C1 (run 362). From the lowest to the highest gas pocket unit at time zero: B (orange line), A (blue line), C (yellow line). The distance of each point is taken with reference to the conduit base. (b) Length of gas pocket units AB (blue line), CA (red line). Orange dots represent the modelled length of the resonator for harmonics shown in (c). (c) Frequency values of different spectral lines (f1, f2, etc.) of the principal group of harmonics (colored dots).*

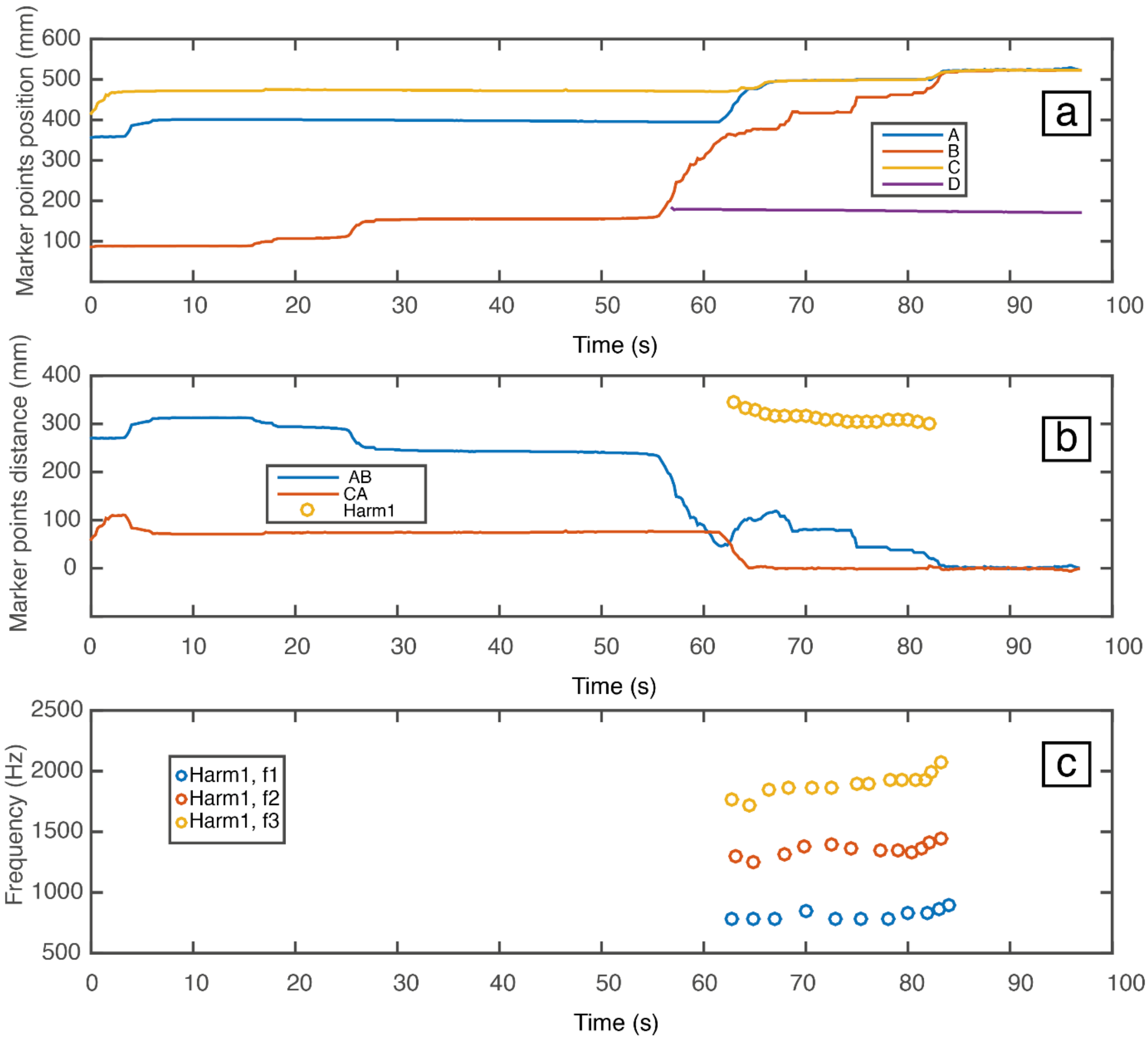

Supplementary Figure 5*: (a) Temporal evolution of gas pocket units through video images. The experimental conditions are: viscosity 1,000 Pa s, gas flux 90x10^{-3} l/s, conduit roughness C1 (run 363). From the lowest to the highest gas pocket unit at time zero: B (orange line), A (blue line), C (yellow line), D (purple line). The distance of each point is taken with reference to the conduit base. (b) Length of gas pocket units AB (blue line), CA (red line). Orange dots represent the modelled length of the resonator for harmonics shown in (c). (c) Frequency values of different spectral lines (f1, f2, etc.) of the principal group of harmonics (colored dots). Note that the open conduit core above gas pockets terminations A and C up to the conduit surface measured at 70 s has a length of ca. 335 cm.*

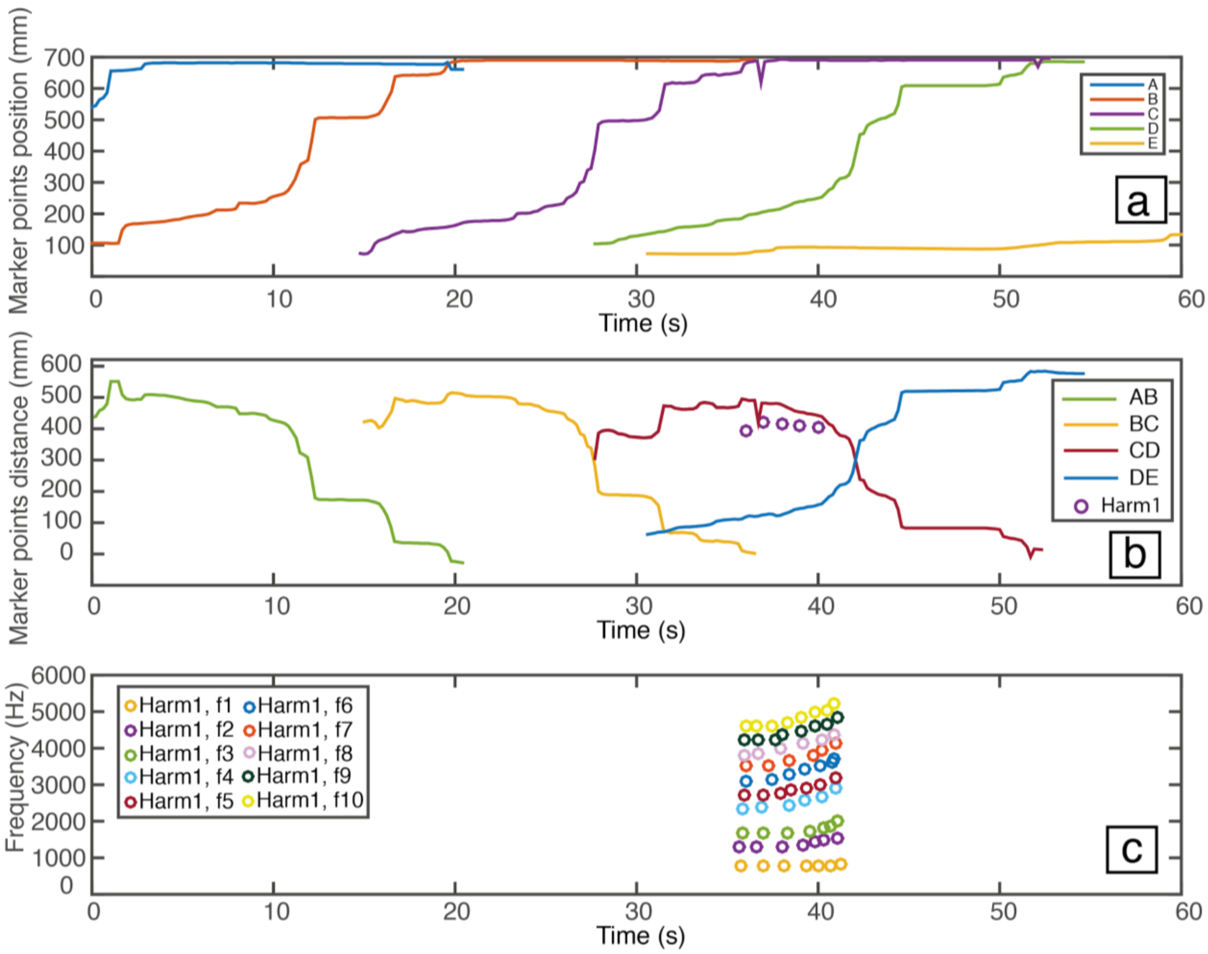

Supplementary Figure 6*: (a) Temporal evolution of gas pockets units through video images. The experimental conditions are: viscosity 100 Pa s, gas flux 180x10^{-3} l/s, conduit roughness C1 (run 269). From the lowest to the highest gas pockets unit at time zero, following a temporal trend: A (blue line), B (orange line), C (purple line), D (green line), E (yellow line). The distance of each point is taken with reference to the conduit base. (b) Length of gas pockets units AB (green line), BC (yellow line), CD (red line) and DE (blue line). Purple dots represent the modelled length of the resonator for harmonics shown in (c). (c) Frequency values of different spectral lines (f1, f2, etc.) of the principal group of harmonics (colored dots).*

Table 1

	Parameters						Adimensional numbers				
	ρ_l (kg/m^3)	η (Pa s)	σ (N/m)	D (m)	D_{churn} (m)	U_{gas} (m/s)	$\pi_1 = \frac{u_{gas*\eta}}{\sigma}$	$\pi_2 = \frac{\varrho\sigma D}{\eta^2}$= Oh^{-2}	$\pi_3 = \frac{D}{Dchurn}$	*Mo*= $\frac{g\eta^4\Delta\rho}{\rho_l{}^2\sigma^3}$	*Re2p* = $\frac{JD\rho_{an}}{\mu}$
This paper	970	100-1,000	0.025	0.03	0.015-0.027	0.04-0.25	1.9*10^{2-} 1.1*10^4	6.2*10^{-5} 6.2*10^{-7}	0.5-0.9	10^{11}-10^{15}	10^{-2}-10^{-3}
Hasan et al. (2019)	950	360	0.025	0.24	---	0.1-0.56	1.8-9.8*10^3	3.8*10^{-5}			
Basaltic volcanoes	2700	100-1,000	0.3	15	2-14	0.5-5	1.5*10^2 1.5*10^4	1.46*10^{-2} - 1.46	0.13-1	Strombolian activity:10^2-10^{15*}	Weak fountian activity: 10^{-2}-10^{-3}*

A-dimensional P numbers for this paper, Hasan et al. (2019) and basaltic volcanoes. Reynold number of the two phase mixture was computed using J=U_{gas} and calculating ρ_{an} from Seyfriend and Freundt (2000), with a value of air gas density equal to 1.18-5.94 kg/m3 (1-5 bar) and assuming a liquid percentage of 20% along an hypothetical conduit section. The values of Reynold Numbers are relative to weak fountain activity at Etna (La Spina et al. 2021), whereas the Morton Number for Strombolian activity is quoted from Del Bello et al. (2012).

Supplementary Table 1

Experimental name	Viscosity (Pa s)	Gas Flux (120x10^{-3}l/s)	Superficial velocity (m/s)	Conduit geometry C1=Fractal dimension 2 C2=Fractal dimension 2.18 C3=Fractal dimension 2.99
Run 312	1,000	120	0.17	C1
Run 353	1,000	180	0.25	C1
Run 309	1,000	180	0.25	C2
Run 324	1,000	30	0.04	C2
Run 361	1,000	120	0.17	C1
Run 362	1,000	90	0.11	C1
Run 363	1,000	90	0.11	C1
Run 269	100	180	0.25	C1

Supplementary Table 1: *Experimental conditions of the subset of gliding episodes addressed in this paper.*

Supplementary video 1: Degassing pattern of run 312 featuring conduit geometry C2, analogue magma viscosity of 1,000 Pas and gas flux equal to $120x10^{-3}$ l/s Note that the experimental conduit was orientated along the vertical direction.

Supplementary video 2: Degassing pattern of run 353 featuring conduit geometry C1, analogue magma viscosity of 1,000 Pas and gas flux equal to $180x10^{-3}$ l/s Note that the experimental conduit was orientated along the vertical direction.

Supplementary video 3: Degassing pattern of run 309 featuring conduit geometry C2, analogue magma viscosity of 1,000 Pas and gas flux equal to $180x10^{-3}$ l/s Note that the experimental conduit was orientated along the vertical direction.

Supplementary video 4: Degassing pattern of run 324 featuring conduit geometry C2, analogue magma viscosity of 1,000 Pas and gas flux equal to $30x10^{-3}$ l/s Note that the experimental conduit was orientated along the vertical direction.

Supplementary video 5: Degassing pattern of run 361 featuring conduit geometry C1, analogue magma viscosity of 1,000 Pas and gas flux equal to $120x10^{-3}$ l/s Note that the experimental conduit was orientated along the vertical direction.

Supplementary video 6: Degassing pattern of run 362 featuring conduit geometry C1, analogue magma viscosity of 1,000 Pas and gas flux equal to $90x10^{-3}$ l/s Note that the experimental conduit was orientated along the vertical direction.

Supplementary video 7: Degassing pattern of run 363 featuring conduit geometry C1, analogue magma viscosity of 1,000 Pas and gas flux equal to 90×10^{-3} l/s Note that the experimental conduit was orientated along the vertical direction.

Supplementary video 7: Degassing pattern of run 269 featuring conduit geometry C1, analogue magma viscosity of 100 Pas and gas flux equal to 180×10^{-3} l/s Note that the experimental conduit was orientated along the vertical direction.